A Letters Journal Exploring the Frontiers of Physics

October 2019

EPL, **128** (2019) 27006
doi: 10.1209/0295-5075/128/27006

www.epljournal.org

Observation of a ferromagnetic-to-paramagnetic phase transition in $Ce_{0.65}Mg_{0.35}Co_3$

Zhengming Zhang[1,2(a)], Wenxia Su[2], Jun Ren[2], Pengtao Cheng[2], Haiming Lu[2], Dunhui Wang[1,2(b)], Qingqi Cao[2], Fang Wang[3], Xiaohong Xu[3] and Youwei Du[1,2,3]

[1] *School of Electronics and Information, Hangzhou Dianzi University - Hangzhou, Zhejiang 310018, China*
[2] *National Laboratory of Solid State Microstructures, Jiangsu Provincial Key Laboratory for Nano Technology, Nanjing University - Nanjing, Jiangsu 210093, China*
[3] *Research Institute of Materials Science & Collaborative Innovation Center for Shanxi Advanced Permanent Magnetic Materials and Technology, Shanxi Normal University - Linfen, Shanxi 041004, China*

received 18 July 2019; accepted in final form 28 October 2019
published online 2 January 2020

PACS 75.30.Kz – Magnetic phase boundaries (including classical and quantum magnetic transitions, metamagnetism, etc.)
PACS 75.40.Cx – Static properties (order parameter, static susceptibility, heat capacities, critical exponents, etc.)
PACS 71.20.Eh – Rare earth metals and alloys

Abstract – $Ce_{1-x}Mg_xCo_3$ are promising candidates for the permanent magnets since they can show ferromagnetism and large anisotropy by substituting Mg for Ce in a paramagnetic $CeCo_3$ compound. In this work, a room-temperature ferromagnetism with a second-order magnetic phase transition is observed in the $Ce_{0.65}Mg_{0.35}Co_3$ (CMC) compound prepared by a cold crucible levitation melting method. Based on the DC magnetization data, the critical phenomenon around the phase transition point (∼308 K) in CMC is investigated and the critical exponents β for spontaneous magnetization, γ for susceptibility and δ for critical isothermal magnetization are determined independently by three different data processing techniques including the modified Arrott plot, Kouvel-Fisher plot, and critical isotherm analysis. It is noteworthy that the magnetizations obey the scaling equation, indicating that the critical parameters including T_c, β, γ and δ are reliable and self-consistent. The calculation of spin interaction with the obtained critical exponents further suggests a long-range ferromagnetic coupling with $J(r) \sim r^{-4.622}$ in CMC.

Introduction. – Permanent magnets are classified as hard ferromagnetic (FM) materials for their strong saturation magnetization and high magnetocrystalline anisotropy energy [1]. Owing to these excellent properties, permanent magnets are essential to the progress of advanced science and high technology and they are in great demand of the markets such as hybrid cars, air conditioners, smartphones, and medical treatment devices [2,3]. Rare-earth–based FM compounds can achieve large saturation magnetization because many $4f$ electrons are unpaired in rare-earth atoms. Furthermore, they also exhibit high values of magnetocrystalline anisotropy energy due to the large spin-orbit coupling of $4f$ electrons in rare-earth elements, which eventually leads to a high coercivity for maintaining the magnetic stability against being demagnetized [4]. Therefore, rare-earth–based permanent magnets, such as $SmCo_5$, Sm_2Co_{17}, and $Nd_2Fe_{14}B$, occupy a large amount of market share. However, in recent years, both the shortage of low-abundant rare-earth resources used in permanent magnets and the increase in their price have made the search for efficient earth-abundant permanent magnets crucial [5,6].

Recently, the paramagnetic (PM) $CeCo_3$, containing the most abundant rare-earth element cerium, has been identified as a promising candidate for a strong permanent magnet by Mg doping [7]. Although Ce is inexpensive and can be easily extracted from the other rare-earth materials [8], Ce-based compounds have not been deployed well because the magnetic moment is lost to some extent after alloying with other compounds. For example, the Ce atom of $Ce_2Fe_{14}B$ is in a mixed valence state of Ce^{+3}/Ce^{+4} [9]

(a) E-mail: zmzhang@hdu.edu.cn
(b) E-mail: wangdh@hdu.edu.cn

and the magnetic moment of Fe atom is decreased because Fe 3d orbits are hybridized with Ce 4f electrons [10]. As for pure $CeCo_3$, it only exhibits Pauli PM characteristics even containing so many FM Co atoms in the system. However, by adding the nonmagnetic element Mg [11,12], the compounds $Ce_{1-x}Mg_xCo_3$ ($0 < x \lesssim 0.467$) can order magnetically with large magnetic anisotropy [7]. In the FM phase, first-principle calculation suggests that the density of states (DOS) at Fermi level is increased and the Stoner criterion is fulfilled by Mg alloying, leading to a FM order in $Ce_{1-x}Mg_xCo_3$ [13]. On the other hand, large magnetic anisotropy in the FM phase stems from the viability of electrons interaction between Co-3d and Ce-4f orbits [13]. By increasing the Mg content, the Curie temperature (T_c) of $Ce_{1-x}Mg_xCo_3$ can be as high as 450 K and the magnetic anisotropy energy can achieve 2.2 MJ/m^3, the same magnitude as Sm_2Co_{17} (4.2 MJ/m^3) and $Nd_2Fe_{14}B$ (4.9 MJ/m^3) [2], indicating they have the potential to be sustainable permanent magnets [7].

Although the origin of magnetism and the anisotropy in the FM phase have been investigated via first-principles calculation, details of the spin interaction and the range of exchange are still unclear, which restricts us to gaining the universality class of the magnetic phase transition in the Mg-doped ferromagnet $Ce_{1-x}Mg_xCo_3$. As shown in previous studies, analyzing the critical phenomena around T_c can provide many information such as the type of magnetic phase transition, correlation length, spin dimension, and exchange decay range [14]. It is commonly known that the critical behavior can be well described by obtaining a set of interrelated critical exponents β, γ, and δ [14]. For a system with the second-order transition, the divergence of correlation length near the phase transition point, *e.g.*, $\xi = \xi_0|(T_c - T)/T_c|^{-\nu}$, results in the correlation of all spin fluctuations, which makes the critical exponents independent of microscopic details [15]. Hence, spontaneous magnetization $M_s(T)$ and inverse initial susceptibility $\chi^{-1}(T)$ obey the universal scaling laws [16]. The critical exponents are defined as follows [16]:

$$M_s(T) = M_0\left(\frac{T_c - T}{T_c}\right)^{\beta} = M_0 t^{\beta} \quad (T < T_c), \qquad (1)$$

$$\chi^{-1}(T) = \Gamma\left(\frac{T - T_c}{T_c}\right)^{\gamma} = \Gamma t^{\gamma} \qquad (T > T_c), \qquad (2)$$

$$M(H) = C(\mu_0 H)^{\frac{1}{\delta}} \qquad (T = T_c), \qquad (3)$$

where $t = |\frac{T-T_c}{T_c}|$ is the reduced temperature; $M(H)$ is the field-dependent magnetization at T_c; M_0, Γ, and C are the critical amplitudes [14].

To explore the critical behavior of Mg-doped $CeCo_3$ when approaching the FM-PM transition, a systematic study of the magnetization is carried out. A room-temperature FM compound $Ce_{0.65}Mg_{0.35}Co_3$ (CMC) is successfully synthesized by a cold crucible levitation melting method. Based on the DC magnetization data, the exponents β, γ, and δ are calculated accurately and the system tends to exhibit a long-ranged spin interaction. We further calculate the decaying distance of exchange coupling based on the obtained critical exponents, which confirms that there is a long-range interaction in CMC.

Experiment. – CMC was prepared by using a cold crucible levitation melting method. Ce and Co were firstly melted in a water-cooled crucible under an argon atmosphere. Then Mg was added to the crucible to allow the formation of CMC. The ingot was turned over and melted many times to obtain homogeneity in its chemical composition. The structure of CMC was characterized by X-ray diffraction (XRD) with Cu K_α radiation at room temperature. The measurement of magnetization was carried out by using a superconducting quantum interferometer device (Quantum Design SQUID). In order to obtain more reliable critical exponents of CMC, the isothermal magnetization curves were measured at different temperatures between 230 and 362 K, and the magnetic field was selected between 0 and 5 T. In order to keep the ambient temperature of the sample stable, a long waiting time was given before formally measuring each isothermal magnetization curve. To accurately calculate the critical exponents in the following sections, the external magnetic field H was converted into the following form, $H_i = H - DM$. The demagnetizing factor D was calculated from the sample geometry that was a shape of an irregular but almost spherical polyhedron.

Results and discussions. –

Structure and magnetism. Figure 1 presents the XRD pattern of CMC. By matching the XRD diffraction peaks with the available database, the crystal of CMC can be clearly indexed as a single rhombohedral phase with the $PuNi_3$-type structure. As shown in the inset of fig. 1, Ce atoms occupy two nonequivalent sites 3a and 6c; Co atoms lie on three nonequivalent sites 3b, 6c and 18h; Mg atoms partially replace Ce atoms at the 6c site [7,11]. Figure 2 illustrates the temperature dependence of magnetization (left axis) for CMC measured under 0.1 T between 200 and 380 K. An obvious FM-PM transition takes place above room temperature in the sample. By calculating the maximum of $|\frac{dM}{dT}|$, the Curie temperature is determined as $T_c \approx 308$ K and in agreement with a previous study [7]. A splitting feature between zero-field–cooled (ZFC) and field-cooled (FC) magnetizations is observed, which illustrates that CMC is crystallized in the FM ground state below T_c but exhibits some degrees of FM cluster behavior. As expected, the adjacent Co atoms show a strong FM exchange interaction at the ground state. However, it is also reported that $Ce_{1-x}Mg_xCo_3$ prefers an antiparallel magnetic moment alignment between Ce and Co atoms [13]. In such a case, the competing couplings of FM and antiferromagnetism (AFM) might lead to FM clusters with a macroscopic ZFC-FC divergence. For further understanding the nature of the magnetism in CMC, we investigate the $\chi^{-1}(T)$ based on the ZFC curve using the Curie-Weiss

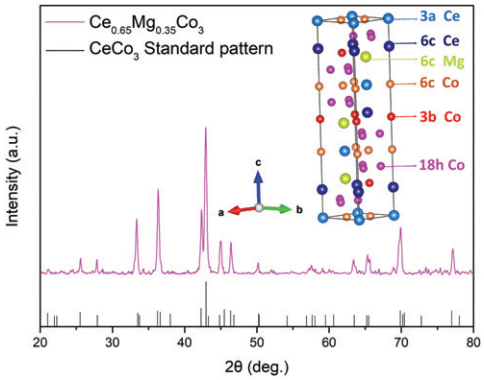

Fig. 1: XRD pattern for CMC, the inset is the crystal structure of CMC.

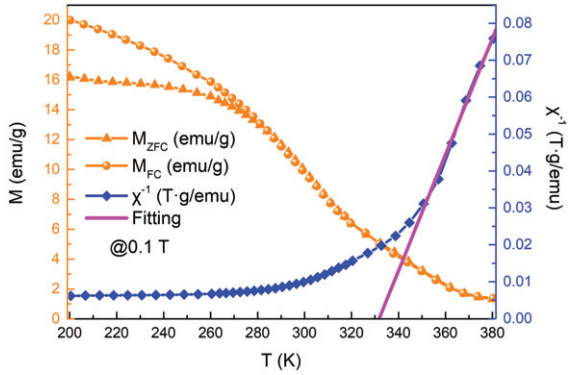

Fig. 2: The temperature dependence of magnetization for CMC obtained under 0.1 T (left axis). The inverse susceptibility as a function of temperature (right axis). The solid line is a linear fit to data based on Curie-Weiss law.

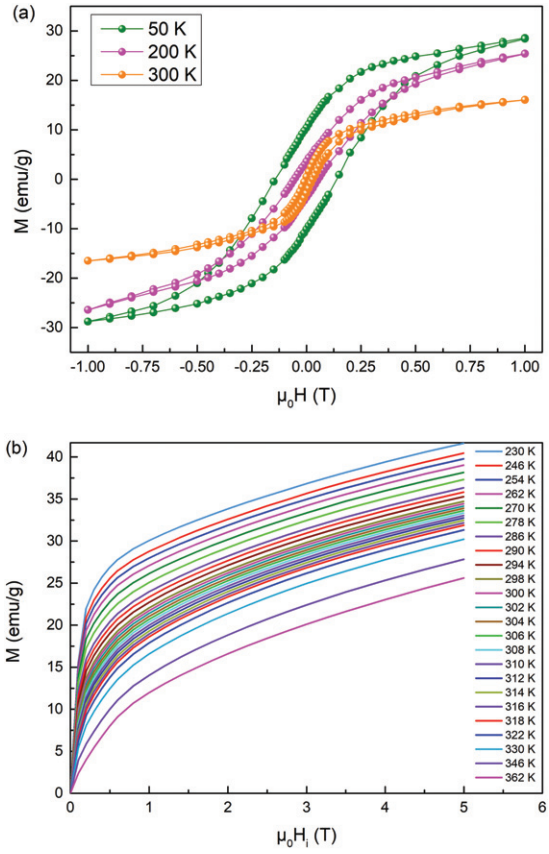

Fig. 3: (a) Magnetic hysteresis loops measured at 50 K, 200 K, and 300 K. (b) Isothermal magnetization curves at different temperatures for CMC.

law. The temperature dependence of inverse susceptibility $\chi^{-1}(T)$ is shown in fig. 2 (right axis), in which the solid line is the data fitted by the Curie-Weiss law. The experimental data in the high-temperature region ($T > 340\,\mathrm{K}$) are well fitted by the Curie-Weiss law, exhibiting a typical PM behavior. Accordingly, by extracting the inverse of the slope and the intercept at the T-axis, the Curie constant C and the Weiss constant θ are determined as $17.55\,\mathrm{emu \cdot K/mol \cdot Oe}$ and $331.3\,\mathrm{K}$, respectively. Here, the positive value of θ suggests the predominant FM exchange interaction in this system. We can calculate the effective magnetic moment approximately using the relation $\mu_{\mathrm{eff}} = \sqrt{\frac{3k_B C}{\mu_B^2 n N_A}} \approx 2.82787 \cdot \sqrt{\frac{C}{3}} \approx 6.839\,\mu_B$, where k_B is the Boltzmann constant, μ_B is the Bohr magneton, N_A is the Avogadro constant, and n is the number of magnetic atoms per formula unit. The effective moment is larger than both the spin moment of Co ions ($\sim 4.90\,\mu_B/\mathrm{Co}^{3+}$) and total moment of Ce ions ($2.54\,\mu_B/\mathrm{Ce}^{3+}$), which also implies that FM clusters might contribute to the magnetization of the sample in the PM state [17]. With decreasing temperature ($T < 340\,\mathrm{K}$), the $\chi^{-1}(T)$ data begins to deviate from the fitting line in the PM state, which further suggests that there exists FM clusters or the bound magnetic polarons related to the defects even in the PM phase of the sample [17–19].

To get more information about the magnetic ground state in this sample, the magnetic hysteresis loops (M-H loops) are measured at 50 K, 200 K, and 300 K. As shown in fig. 3(a), CMC exhibits obvious hysteresis and the coercive field can achieve a value of 0.16 T at 50 K, indicating it can serve as a potential permanent magnet. It should also be noted here that the strong pinning ability with a large coercive field can also contribute to the above ZFC-FC bifurcation. The field-dependent isothermal magnetizations (M-H curves) obtained at various temperatures are shown in fig. 3(b). A series of typical FM and PM M-H curves are observed in CMC. With the increase of temperature, the FM M-H curves gradually transit to PM ones, which also indicates a transition from FM to PM in the sample.

Arrott plot. To deeply understand the magnetic interaction and the FM-PM transition in CMC, we next explore the critical behavior. According to the Arrott plot based on the Landau mean-field theory, the behavior of magnetization around T_c satisfies the following relationship [20]:

$$M^2 = k\left(\frac{\mu_0 H}{M}\right) + b\frac{T_c - T}{T}. \tag{4}$$

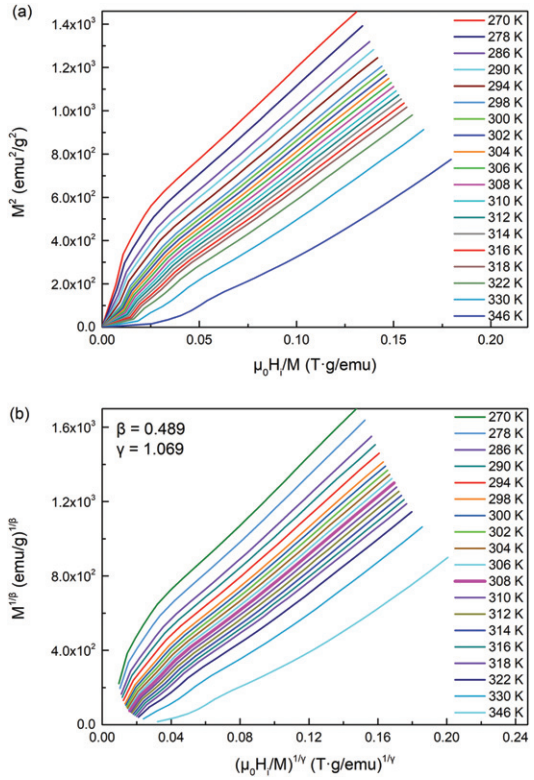

Fig. 4: (a) Arrott plots in the form of M^2 *vs.* $\mu_0 H/M$ measured at different temperatures from 270 to 346 K for CMC. (b) Modified Arrott plots with $\beta = 0.489$ and $\gamma = 1.069$.

For characterizing the magnetic phase transition and calculating β, γ, δ and T_c, one can use the M^2 *vs.* $\frac{\mu_0 H}{M}$ plots based on experimental data [20]. Obviously, if the ferromagnet follows the Landau mean-field theory, the M^2 *vs.* $\frac{\mu_0 H}{M}$ curves around T_c will demonstrate a certain number of parallel lines. Furthermore, one of the lines goes straight through the origin of the coordinates at T_c. At this point, the critical exponents of the system are exactly $\beta = 0.5$, $\gamma = 1$, and $\delta = 3$. Additionally, the method can also give the data of $M_s(T)$ and $\chi^{-1}(T)$ at different temperatures by using the intercepts on the M^2 axis and $\frac{\mu_0 H}{M}$ axis, respectively [21]. As shown in fig. 4(a), the quasi-straight lines of M^2 *vs.* $\frac{\mu_0 H}{M}$ are not strictly parallel to each other, which indicates that the above Arrott plot needs further modification. However, one can easily determine the phase transition order: the negative and positive slopes represent first order and second order, respectively [22]. Here, the slopes of all curves are greater than zero, which implies that the magnetic phase transition in CMC belongs to the second-order system.

Since the M^2 *vs.* $\frac{\mu_0 H}{M}$ relations are not strictly parallel lines, a modified Arrott plot can be alternatively applied to characterize the second-order phase transition system, which is given by [23]

$$M^{1/\beta} = k\left(\frac{\mu_0 H}{M}\right)^{1/\gamma} + b\frac{T_c - T}{T}. \tag{5}$$

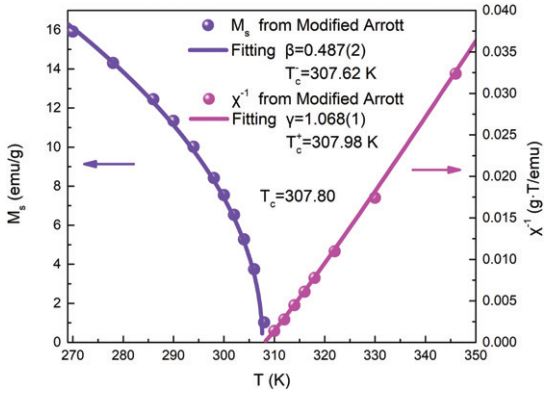

Fig. 5: Temperature dependence of the spontaneous magnetization M_s (left axis) and inverse initial susceptibility χ^{-1} (right axis) which are obtained from the high-field extrapolation of modified Arrott plots.

We use a self-consistent method to calculate β and γ [15]. Firstly, the high field data of the Arrott plots are extrapolated linearly, and the intersection points of the M^2 and $\frac{\mu_0 H}{M}$ axes yield the starting data of $M_s(T)$ and $\chi(T)$, which are used to calculate β and γ based on eq. (1) and eq. (2), respectively. Using these critical exponents, the modified Arrott $M^{1/\beta}$ *vs.* $(\frac{\mu_0 H}{M})^{1/\gamma}$ curves are plotted. By linearly extrapolating the high-field data to the axis, a new set of temperature-dependent spontaneous magnetization and susceptibility is obtained, which yields new values of β and γ [24]. The above fitting method is iterated several times until a pair of stable exponents β and γ are generated. Follow this method, we obtain a series of parallel lines at high fields around T_c as shown in fig. 4(b), where $\beta = 0.489$ and $\gamma = 1.069$. Of course, we also observe a slight bending of the data in the low field, which is the average result of domains magnetized in different directions. Figure 5 presents the final temperature dependence of $M_s(T)$ and $\chi^{-1}(T)$, which gives $\beta = 0.4872$, $T_c^- = 307.62$ K, and $\gamma = 1.0681$, $T_c^+ = 307.98$ K according to eq. (1) and eq. (2), respectively. Based on the values of T_c^+ and T_c^-, the critical temperature is then calculated as $T_c = \frac{T_c^- + T_c^+}{2} = 307.80$ K.

Kouvel-Fisher plot. We can also use another method developed by Kouvel and Fisher (KF) to determine β and γ more accurately [25]. According to the KF method, data can be processed by the following two equations:

$$M_s(T)\left(\frac{\mathrm{d}M_s(T)}{\mathrm{d}T}\right)^{-1} = \frac{T - T_c^-}{\beta}, \tag{6}$$

$$\chi^{-1}(T)\left(\frac{\mathrm{d}\chi^{-1}(T)}{\mathrm{d}T}\right)^{-1} = \frac{T - T_c^+}{\gamma}. \tag{7}$$

The critical exponents near the Curie point are considered as temperature-independent values, both $M_s(T)(\frac{\mathrm{d}M_s(T)}{\mathrm{d}T})^{-1}$ and $\chi^{-1}(T)(\frac{\mathrm{d}\chi^{-1}(T)}{\mathrm{d}T})^{-1}$ have a linear relationship with temperature. Thus, by fitting their linear lines around T_c, we can get the values of β and γ from

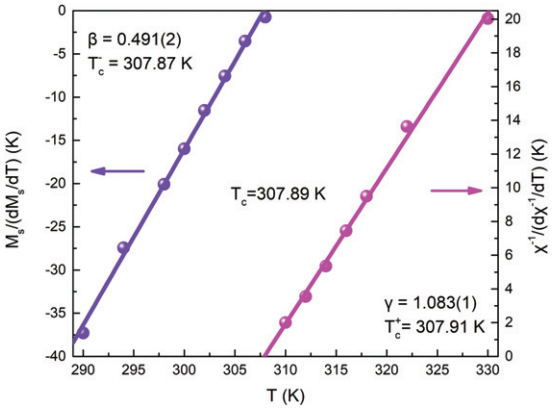

Fig. 6: Kouvel-Fisher plot of spontaneous magnetization M_s (left axis) and inverse initial susceptibility χ^{-1} (right axis) for CMC.

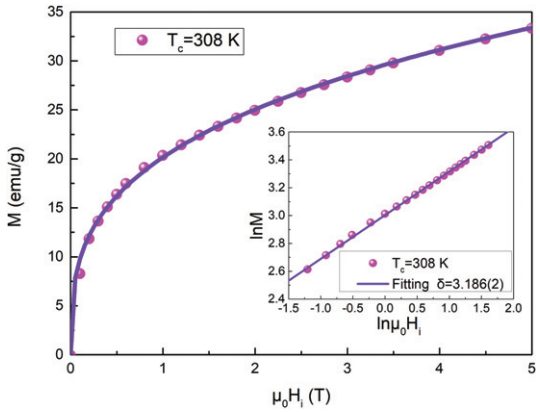

Fig. 7: Critical isotherm of M *vs.* H at T_c of 308 K. The inset shows the same on the ln-ln scale and the straight line is the linear fit following eq. (3).

the inverse slopes of the two lines. In addition, the KF method does not require an *a priori* value of the critical temperature, as long as the intercept of the two fitting lines on the T axis can be obtained. By using $M_s(T)$ and $\chi^{-1}(T)$ from the modified Arrott plot, the KF plots are shown in fig. 6. Based on the fitted solid lines, the critical parameters for CMC are determined as $\beta = 0.4912$ and $\gamma = 1.0831$ with $T_c = \frac{T_c^- + T_c^+}{2} = 307.89\,\mathrm{K}$ by the KF method. It is shown that these values of β, γ and T_c agree well with those derived from the modified Arrott plot, suggesting that they are self-consistent.

Critical isotherm analysis. According to the Widom scaling theory [16], the third exponent δ can be determined by analyzing the isothermal magnetization curve measured at critical temperature T_c. From the above analysis, the critical temperature of the system is ∼308 K. Here, we choose the critical isothermal magnetization data at 308 K for plotting the $\ln M$ *vs.* $\ln \mu_0 H$ curve, as shown in fig. 7. By fitting the data of $\ln M$ *vs.* $\ln \mu_0 H$ linearly, the value of δ is obtained as 3.186 from the inverse of the slope following eq. (3). On the other hand, we can also use the Widom scaling relation $\delta = 1 + \frac{\gamma}{\beta}$ [26] to calculate δ. By using the obtained values of β and γ, the third critical exponent is determined as $\delta = 3.192$ and $\delta = 3.205$ for the modified Arrott plots and KF method, respectively. The calculated results of the Widom scaling relation agree well with those of the critical isotherm analysis, which indirectly suggests that the estimated exponents and T_c for CMC using modified Arrott plots and the KF method are reliable and intrinsic.

Scaling equation of state. For further verifying the reliability of the critical parameters including β, γ, δ and T_c, we check whether the magnetic data satisfy the following equation:

$$m = f_{\pm}(h), \tag{8}$$

where $f_+(h)$ and $f_-(h)$ are two different analytical functions; $m = t^{-\beta}M(H,t)$ is the scaled magnetization; $h = t^{-(\beta+\gamma)}H$ is the scaled field [18]. Here, the positive sign

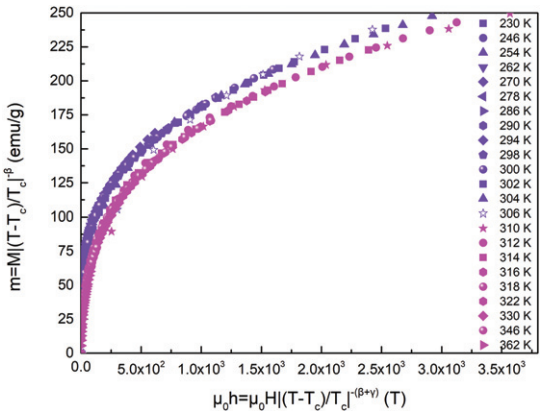

Fig. 8: The scaled magnetization is plotted as a function of the scaled field following eq. (8). The plot shows that all the data fall onto one branch curve for $T < T_c$ and the other for $T > T_c$.

and negative sign represent a temperature higher and lower than the Curie temperature, respectively. Apparently, if there is a true scale relationship and the critical parameters obtained are accurate, then all magnetic data will converge to two curves, one is the data below the critical point, the other is the data above the critical point. By using the relevant experimental data and critical parameters, the universal scaling curve m *vs.* h is obtained in fig. 8. Obviously, the scaling M-H data are distributed on only two different curves for a temperature higher and lower than the Curie temperature, respectively. This phenomenon shows that the interaction at the critical region is properly renormalized according to the scaling equation of state [18], which also implies that the critical parameters are accurate within the experimental error range.

Spin interaction. The estimated critical exponents of CMC are listed in table 1, in which the data from different methods and a few data from different theoretical models in the literature are compared [27]. It is shown that the obtained exponents are close to the Landau mean-field theory, indicating that the FM interaction in CMC

Table 1: Comparison of the critical parameters of $Ce_{0.65}Mg_{0.35}Co_3$ with different theoretical models.

Technique	β	γ	δ	T_c
Modified Arrot plot	0.4872	1.0681	3.192*	307.80
Kouvel-Fisher plot	0.4912	1.0831	3.205*	307.89
Critical isotherm			3.186	308
Mean field [27]	0.500	1.00	3.00	\
3D Heisenberg [27]	0.365	1.386	4.80	\
3D Ising [27]	0.325	1.241	4.82	\

*Calculated from the Widom scaling relation $\delta = 1 + \gamma/\beta$.

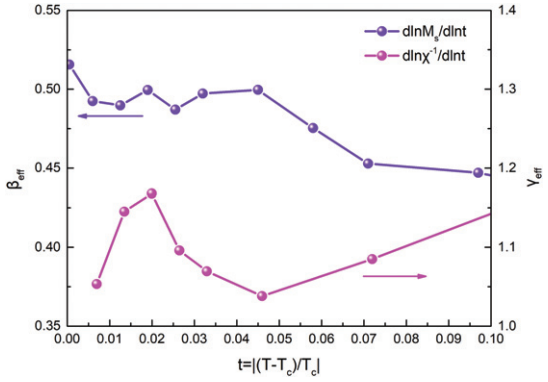

Fig. 9: Effective exponents β_{eff} below T_c and γ_{eff} above T_c as a function of the reduced temperature t in CMC.

is long-ranged. However, we can also see that β and γ deviate slightly from the theoretical values. In addition, if there are many competing couplings or disorders in a magnetic system, the exponents will exhibit some systematic trends or critical crossover phenomena near the phase transition point [28]. In view of this, it is vital to obtain the following temperature-dependent effective exponents:

$$\beta_{\text{eff}}(t) = \frac{\mathrm{d}\ln M_s(t)}{\mathrm{d}\ln t}, \quad \gamma_{\text{eff}}(t) = \frac{\mathrm{d}\ln \chi^{-1}(t)}{\mathrm{d}\ln t}. \tag{9}$$

As shown in fig. 9, both $\beta_{\text{eff}}(t)$ and $\gamma_{\text{eff}}(t)$ are basically nonmonotonic, implying that critical exponents do not belong to any known universality class, including 3D Ising class, 3D Heisenberg class, and mean-field class [24]. This nonmonotonic change probably originates from the competing interactions of the FM exchange between adjacent Co atoms and the AFM exchange between Ce and Co atoms, which is consistent with the splitting phenomenon between ZFC and FC curves. Nevertheless, since the correlation length near the critical point is divergent and the critical exponents are independent of microscopic details [15], our obtained critical exponents are intrinsic.

According to the theory of renormalization group (RG), the long-range attraction decays as $J(r) \sim r^{-(d+\sigma)}$, where r and d denote the distance and the dimension of space, respectively [14]. The constant σ in the long-ranged system satisfies the following formula [14]:

$$\gamma = 1 + \frac{4}{d}\frac{n+2}{n+8}\Delta\sigma + \frac{8(n+2)(n-4)}{d^2(n+8)^2} \times \left[1 + \frac{2G(\frac{d}{2})(7n+20)}{(n-4)n+8}\right]\Delta\sigma^2, \tag{10}$$

where $\Delta\sigma = (\sigma - \frac{d}{2})$, $G(\frac{d}{2}) = 3 - \frac{1}{4}(\frac{d}{2})^2$, and n is the dimension of spin. The equation is applicable to $\frac{d}{2} \leq \sigma \leq 2$ [29]. When the dimension of space d is 3, the long-range interaction then decays as $J(r) \sim r^{-(3+\sigma)}$ with the constant σ between 1.5 and 2. In such a case, $J(r)$ is somewhere between $r^{-4.5}$ and r^{-5} and the value of σ governs the universality classes with different sets of exponents. If σ is less than 1.5, the Landau mean-field theory can be used to describe magnetic behavior and $J(r)$ decreases more slowly than $\sim r^{-4.5}$, leading to a longer exchange range [29]. If σ exceeds 2, the conditions for the 3D isotropic Heisenberg model are satisfied, expecting that $J(r)$ decays sharply faster than $\sim r^{-5}$ and the exchange range is thereby shortened [29]. Herein, $\sigma = 1.622$ is obtained reasonably according to eq. (10) with the value of γ, and $J(r)$ thereby decays as $\sim r^{-4.622}$ in CMC. It is noticed that the obtained σ belongs to the long-range interaction and $J(r)$ is close to the Landau mean-field theory. In fact, first-principle calculation suggests that DOS at the Fermi level is governed by the Co 3*d* orbits in $Ce_{2/3}Mg_{1/3}Co_3$ [13]. However, all the *d* orbits are hybridized with adjacent atoms, resulting in band broadening at the Fermi level [13]. Therefore, the 3*d* electrons of Co atoms exhibit some degree of itinerancy. Moreover, it is reported that the Rhodes-Wolfarth ratio (RWR) can be applied to distinguish between itinerant magnetism and localized magnetism, *e.g.*, RWR = 1, the electrons are localized; RWR > 1, there exists the itinerant FM in the sample [30]. Based on the Rhodes and Wolfarth theory [30], RWR is defined as μ_C/μ_S, where μ_C and μ_S are related to the number of moving carriers and saturation magnetization, respectively. For CMC, by using the previously obtained μ_{eff}, the value of μ_C can be determined from $\mu_{\text{eff}}^2 = \mu_C(\mu_C + 2)$, which yields $\mu_C = 5.91\mu_B$. The saturation magnetic moment per Co atom μ_S of CMC is about $\sim 0.68\,\mu_B$. Therefore, the RWR is calculated as 8.69, suggesting an itinerant character of spin interaction with long-range $J(r)$ in the Mg-doped $CeCo_3$ system.

Conclusion. – In summary, we observe a second-order FM-PM transition in CMC. The FM order in this compound is induced by Mg doping into the Ce site of the Pauli paramagnet $CeCo_3$. The critical phenomenon around T_c of 308 K in CMC is systematically studied. By using reliable data processing methods, including the Arrott plot (modified), KF technique, and critical isotherm method, the critical exponent β for spontaneous magnetization, γ for susceptibility and δ for critical isothermal magnetization are obtained accurately. More importantly, these self-consistent critical exponents satisfy

the scaling equation of the state well, suggesting that they are reliable within the experimental error range. It is also observed that the spin decay range of the system has the form $J(r) \sim r^{-4.622}$, confirming a long-ranged coupling in the itinerant FM compound CMC. The magnetic phase transition in Mg-doped $CeCo_3$ may also be used in magnetoresistance, magnetic sensors and other fields.

* * *

This work was supported by the National Key R&D Program of China (Grant No. 2017YFB0702701), and the Fundamental Research Funds for the Provincial Universities of Zhejiang (Grant No. GK199900299012-012).

REFERENCES

[1] Buschow K. H. J., *Rep. Prog. Phys.*, **54** (1991) 1123.
[2] Coey J. M. D., *IEEE Trans. Magn.*, **47** (2011) 4671.
[3] Coey J. M. D., *Scr. Mater.*, **67** (2012) 524.
[4] Pandey T., Du M.-H. and Parker D. S., *Phys. Rev. Appl.*, **9** (2018) 034002.
[5] Lamichhane T. N., Taufour V., Masters M. W., Parker D. S., Kaluarachchi U. S., Thimmaiah S., Bud'ko S. L. and Canfield P. C., *Appl. Phys. Lett.*, **109** (2016) 092402.
[6] Budrikis Z., *Nat. Rev. Mater.*, **3** (2018) 18018.
[7] Lamichhane T. N., Taufour V., Palasyuk A., Lin Q., Bud'ko S. L. and Canfield P. C., *Phys. Rev. Appl.*, **9** (2018) 024023.
[8] Xie F., Zhang T. A., Dreisinger D. and Doyle F., *Miner. Eng.*, **56** (2014) 10.
[9] Capehart T. W., Mishra R. K., Meisner G. P., Fuerst C. D. and Herbst J. F., *Appl. Phys. Lett.*, **63** (1993) 3642.
[10] Pathak A. K., Khan M., Gshneidner K. A., Mccallum R. W., Zhou L., Sun K., Dennis K. W., Zhou C., Pinkerton F. E., Kramer M. J. and Pecharsky V. K., *Adv. Mater.*, **27** (2015) 2663.
[11] Denys R. V., Riabov A. B., Černý R., Koval'chuk I. V. and Zavaliy I. Y., *J. Solid State Chem.*, **187** (2012) 1.
[12] Shtender V. V., Denys R. V., Paul-Boncour V., Zavaliy I. Y., Verbovytskyy Y. V. and Taylor D. D., *J. Alloys Compd.*, **695** (2017) 1426.
[13] Pandey T. and Parker D. S., *Phys. Rev. Appl.*, **10** (2018) 034038.
[14] Lin S., Lv H., Lin J., Huang Y., Zhang L., Song W., Tong P., Lu W. and Sun Y., *Phys. Rev. B*, **98** (2018) 014412.
[15] Mira J., Rivas J., Vázquez M., García-Beneytez J. M., Arcas J., Sánchez R. D. and Señarís-Rodríguez M. A., *Phys. Rev. B*, **59** (1999) 123.
[16] Stanley H. Eugene, *Introduction to Phase Transitions and Critical Phenomena* (Oxford University Press, New York) 1971.
[17] Phong P., Ngan L., Dang N., Nguyen L., Nam P., Thuy D., Tuan N., Bau L. and Lee I., *J. Magn. Magn. Mater.*, **449** (2018) 558.
[18] Khan N., Midya A., Mydeen K., Mandal P., Loidl A. and Prabhakaran D., *Phys. Rev. B*, **82** (2010) 064422.
[19] Zhang L., Wang B., Sun Y., Tong P., Fan J., Zhang C., Pi L. and Zhang Y., *Phys. Rev. B*, **85** (2012) 104419.
[20] Arrott A., *Phys. Rev.*, **108** (1957) 1394.
[21] Sambasiva Rao M. and Kaul S. N., *J. Magn. Magn. Mater.*, **147** (1995) 149.
[22] Banerjee B. K., *Phys. Lett.*, **12** (1964) 16.
[23] Arrott A. and Noakes J. E., *Phys. Rev. Lett.*, **19** (1967) 786.
[24] Sabyasachi S., Bhattacharyya A., Majumdar S., Giri S. and Chatterji T., *J. Alloys Compd.*, **577** (2013) 165.
[25] Kouvel J. S. and Fisher M. E., *Phys. Rev.*, **136** (1964) A1626.
[26] Widom B., *J. Chem. Phys.*, **43** (1965) 3892.
[27] Kaul S. N., *J. Magn. Magn. Mater.*, **53** (1985) 5.
[28] Pramamnik A. K. and Banerjee A., *Phys. Rev. B*, **79** (2009) 214426.
[29] Tateiwa N., Pospíšil J., Haga Y. and Yamamoto E., *Phys. Rev. B*, **97** (2018) 064423.
[30] Rhodes P., Wohlfarth E. P. and Jones H., *Proc. R. Soc. Lond. A*, **273** (1963) 247.